

# The AGB superwind speed at low metallicity

Jonathan R. Marshall<sup>1\*</sup>, Jacco Th. van Loon<sup>1</sup>, Mikako Matsuura<sup>2</sup>,  
Peter R. Wood<sup>3</sup>, Albert A. Zijlstra<sup>2</sup> and Patricia A. Whitelock<sup>4</sup>

<sup>1</sup>*Astrophysics Group, School of Chemistry and Physics, Keele University, Staffordshire, ST5 5BG, United Kingdom*

<sup>2</sup>*UMIST, Department of Physics, P.O. Box 88, Manchester, M60 1QD, United Kingdom*

<sup>3</sup>*Research School of Astronomy and Astrophysics, Australian National University, Cotter Road, Weston Creek, ACT 2611, Australia*

<sup>4</sup>*South African Astronomical Observatory, P.O. Box 9, 7935 Observatory, South Africa*

Submitted 2004

## ABSTRACT

We present the results of a survey for OH maser emission at 1612 MHz from dust-enshrouded AGB stars and supergiants in the LMC and SMC, with the Parkes radio telescope, aimed at deriving the speed of the superwind from the double-peaked OH maser profiles. Out of 8 targets in the LMC we detected 5, of which 3 are new detections — no maser emission was detected in the two SMC targets. We detected for the first time the redshifted components of the OH maser profile in the extreme red supergiant IRAS 04553–6825, confirming the suspicion that its wind speed had been severely underestimated. Despite a much improved spectrum for IRAS 04407–7000, which was known to exhibit a single-peaked OH maser, no complementary peak could be detected. The new detection in IRAS 05003–6712 was also single-peaked, but for two other new detections, IRAS 04498–6842 and IRAS 05558–7000, wind speeds could be determined from their double-peaked maser profiles. The complete sample of known OH/IR stars in the LMC is compared with a sample of OH/IR stars in the galactic centre. The LMC sources generally show a pronounced asymmetry between the bright blueshifted maser emission and weaker redshifted emission, which we attribute to the greater contribution of amplification of radiation coming directly from the star itself as the LMC sources are both more luminous and less dusty than their galactic centre counterparts. We confirm that the OH maser strength is a measure of the dust (rather than gas) mass-loss rate. At a given luminosity or pulsation period, the wind speed in LMC sources is lower than in galactic centre sources, and the observed trends confirm simple radiation-driven wind theory if the dust-to-gas ratio is approximately proportional to the metallicity.

**Key words:** masers – stars: AGB and post-AGB – stars: mass-loss – supergiants – stars: winds, outflows – Magellanic Clouds

## 1 INTRODUCTION

Asymptotic Giant Branch (AGB) stars lose  $\sim 35$  to  $85\%$  of their mass before ending up as white dwarfs. Much of this mass loss takes place near the tip of the AGB during the superwind stage, at mass-loss rates of up to  $\dot{M} \sim 10^{-4} \text{ M}_{\odot} \text{ yr}^{-1}$  (van Loon et al. 1999, 2003) leading to the early cessation of their stellar evolution and resulting in chemical enrichment of the interstellar medium (ISM). The mass loss occurs in the form of a stellar wind reaching typical outflow velocities of 5 to 30 km s<sup>-1</sup>. These winds are driven by radiation pressure on dust grains that form at a height of several stellar radii (Goldreich & Scoville 1976) in the

presence of strong radial pulsation of the base of the stellar atmosphere. Likewise, more massive stars ( $M_{\text{ZAMS}} \gtrsim 8 \text{ M}_{\odot}$ ) may pass through a red supergiant phase and lose mass in a similar manner.

During the superwind stage the circumstellar dust envelope becomes opaque at visual wavelengths, but the absorbed stellar light is re-radiated at infrared (IR) wavelengths. The resulting spectral energy distribution may be modelled in order to derive the mass-loss rate, provided we know the dust-to-gas ratio, dust grain properties, stellar luminosity and effective temperature, and outflow kinematics. Data on Magellanic Cloud and galactic dust-enshrouded AGB stars are consistent with a dust-to-gas ratio which depends linearly on metallicity, without a strong metallicity dependence of the total (gas+dust) mass-loss rate (van Loon 2000). This relies on the validity of simple dust-driven wind

\* E-mail: jrm@astro.keele.ac.uk

**Table 1.** The target sample plus the detections from Wood et al. (1992). Bolometric magnitudes  $M_{\text{bol}}$ , pulsation periods  $P$ , K-band pulsation amplitudes  $\Delta K$ , K-band magnitudes and colours  $J - K$  are from Whitelock et al. (2003), *IRAS* 25  $\mu\text{m}$  flux densities  $F_{25}$  (not colour-corrected) are from Trams et al. (1999), and spectral types are from van Loon et al. (in preparation), except where noted otherwise. We adopt distances to the SMC and LMC of 50 and 60 kpc, respectively (distance moduli of 18.5 and 18.9 mag, respectively). Also listed are the previously detected OH masers, and whether we detected OH maser emission here (no entry means never tried).

| Object name   | Alternative name | $M_{\text{bol}}$<br>(mag) | $P$<br>(mag)      | $\Delta K$<br>(days) | $K$<br>(mag)       | $F_{25}$<br>(Jy)   | $J - K$           | Spectral type      | Previous OH      | This work OH |
|---|------------------|---------------------------|-------------------|----------------------|--------------------|--------------------|-------------------|--------------------|------------------|--------------|
| <i>SMC</i>  |                  |                           |                   |                      |                    |                    |                   |                    |                  |              |
| IRAS 00483–7347   | LI-SMC 61        | −7.20 <sup>8</sup>        | 1200 <sup>8</sup> | 0.61 <sup>8</sup>    | 9.10 <sup>3</sup>  | 0.46 <sup>3</sup>  | 3.01 <sup>3</sup> | late-M             |                  | no           |
| IRAS 00591–7307   | HV 11417         | −8.30 <sup>2</sup>        | $\gtrsim 1000^1$  | $> 2.00$             | 8.30 <sup>3</sup>  | 0.10 <sup>3</sup>  | 1.33 <sup>3</sup> | M5e I <sup>1</sup> |                  | no           |
| <i>LMC</i>  |                  |                           |                   |                      |                    |                    |                   |                    |                  |              |
| IRAS 04407–7000   | LI-LMC 4         | −7.11                     | 1199              | 1.23                 | 8.79               | 0.76               | 2.34              | M7.5               | yes <sup>6</sup> | yes          |
| IRAS 04498–6842   | LI-LMC 60        | −7.72                     | 1292              | 1.30                 | 8.08               | 0.89               | 1.86              | M10                |                  | yes          |
| IRAS 04509–6922   | LI-LMC 77        | −7.28                     | 1292              | 1.45                 | 8.59               | 0.86               | 2.21              | M10 <sup>6</sup>   | no <sup>9</sup>  | no           |
| IRAS 04516–6902   | LI-LMC 92        | −7.11                     | 1091              | 1.41                 | 8.72               | 0.55               | 2.32              | M9 <sup>6</sup>    |                  | no           |
| IRAS 04553–6825   | WOH G064         | −9.19 <sup>5</sup>        | 841               | 0.34                 | 7.09               | 13.53              | 2.60 <sup>4</sup> | M7.5               | yes <sup>9</sup> | yes          |
| IRAS 05003–6712   | LI-LMC 0297      | −6.20                     | 883               | 1.59                 | 9.95               | 0.33               | 2.95              | M9                 |                  | yes          |
| IRAS 05294–7104   | LI-LMC 1153      | −6.79                     | 1079              | 1.20                 | 9.21               | 0.56               | 2.97              | M8                 |                  | no           |
| IRAS 05558–7000   | LI-LMC 1790      | −6.97                     | 1220              | 1.42                 | 9.25               | 0.80               | 3.27              |                    |                  | yes          |
| <i>Sample from Wood et al. (1992) — excluding IRAS 04553–6825</i> |                  |                           |                   |                      |                    |                    |                   |                    |                  |              |
| IRAS 04545–7000   | LI-LMC 159       | −6.56                     | 1216              | 1.57                 | 10.13              | 0.83               | 5.70 <sup>9</sup> |                    | yes <sup>9</sup> |              |
| IRAS 05280–6910   | NGC 1984-IRS1    | −7.75 <sup>9</sup>        |                   |                      | 8.19 <sup>9</sup>  | 24.18 <sup>7</sup> |                   |                    | yes <sup>9</sup> |              |
| IRAS 05298–6957   | LI-LMC 1164      | −6.72 <sup>9</sup>        | 1280 <sup>9</sup> | 2.00 <sup>9</sup>    | 10.29 <sup>9</sup> | 1.38               | 3.54 <sup>9</sup> |                    | yes <sup>9</sup> |              |
| IRAS 05329–6708   | LI-LMC 1286      | −6.95                     | 1262              | 1.50                 | 9.90               | 1.23               | 5.10 <sup>9</sup> |                    | yes <sup>9</sup> |              |
| IRAS 05402–6956   |                  | −6.77                     | 1393              | 1.80                 | 10.40              | 1.02               | 4.46 <sup>9</sup> |                    | yes <sup>9</sup> |              |

References: <sup>1</sup> Elias, Frogel & Humphreys (1980), <sup>2</sup> Elias, Frogel & Humphreys (1985), <sup>3</sup> Groenewegen & Blommaert (1998), <sup>4</sup> Trams et al. (1999), <sup>5</sup> van Loon et al. (1999), <sup>6</sup> van Loon et al. (1998a), <sup>7</sup> van Loon et al. (2001b), <sup>8</sup> Whitelock et al. (1989), <sup>9</sup> Wood et al. (1992).

theory, in which the wind speed,  $v_{\text{exp}}$ , depends on the dust-to-gas ratio,  $\psi$ , and luminosity,  $L$ , as (van Loon 2000; cf. Habing, Tignon & Tielens 1994; Elitzur & Ivezić 2001):

$$v_{\text{exp}} \propto \psi^{1/2} L^{1/4}. \quad (1)$$

It is thus of importance, both for deriving accurate mass-loss rates as well as for understanding the mass-loss mechanism, to measure wind speeds for stars of different luminosity and metallicity.

The wind speed may be measured from molecular emission line profiles at radio and (sub)mm wavelengths. This is best done for the abundant CO molecule, but its lines are too weak to detect outside the local galactic disk with presently available observatories. Oxygen-rich dust-enshrouded AGB stars (invariably of M spectral type) may also exhibit intense maser emission from the stimulated re-emission of stellar and circumstellar radiation by SiO, H<sub>2</sub>O and/or OH molecules. These masers are radially stratified due to the spatial separation of the molecules in the outflowing circumstellar envelope (see Habing (1996) for a review). SiO is easily condensed into dust grains and therefore is abundant only in the dust-free inner cavity close to the star. Its maser emission is tangentially amplified resulting in a single peak which can be used to determine the stellar velocity. H<sub>2</sub>O masers originate in the dust formation zone. In Miras these are predominantly amplified tangentially, providing another means of measuring the stellar velocity, but in the more extreme OH/IR stars also radial amplification is effective, resulting in a double-peaked line profile from which the outflow velocity can be measured (Takaba et al. 1994). OH is formed by the dissociation of H<sub>2</sub>O by interstellar UV radiation (Goldreich & Scoville 1976). As the OH maser emis-

sion is radially amplified it provides a means for measuring the speed of the fully developed wind (Elitzur, Goldreich & Scoville 1976) — as opposed to the H<sub>2</sub>O masers which probe a region where the wind has not yet reached its final speed (Richards, Yates & Cohen 1998, 1999).

OH masers have been widely detected in galactic metal-rich samples. The best opportunities to investigate the wind speed in a low-metallicity environment are provided by the Large Magellanic Cloud (LMC) and Small Magellanic Cloud (SMC), with metallicities of the intermediate-age stellar populations of  $\sim \frac{1}{3}$  and  $\sim \frac{1}{5}$  solar respectively. The Magellanic Clouds have the additional advantage that their distances are reasonably well known, and hence the dependence of the wind speed on stellar luminosity can be determined. Prior to this study, only seven identified OH/IR stars were known in the LMC, of which five are AGB stars (the other two are supergiants), and none in the SMC. Amongst the five AGB stars, one was detected as a single-peaked OH maser line, and only one showed an uncomplicated “classical” double-peaked profile yielding a reliable value for its wind speed. We here present new detections of magellanic OH/IR stars, and an analysis of the dependence of the superwind speed on stellar luminosity and metallicity.

## 2 DESCRIPTION OF THE SAMPLE

The first maser searches of magellanic dust-enshrouded AGB stars and red supergiants (Wood et al. 1992; van Loon et al. 2001b) were based on *IRAS*-selected point sources (e.g. Loup et al. 1997) at a time when not much was known about the nature of these *IRAS* sources. Since the mid-1990s, in

**Table 2.** OH maser detections, with the heliocentric velocities of the blue and red peaks (where identified), corresponding wind speed  $v_{\text{exp}}$  from the separation of the peaks, peak flux density and integrated flux  $F_{\text{int}}$ . The rms noise levels in the flux densities and in the integrated fluxes are also listed as  $\sigma$  and  $\sigma_{\text{int}}$ , respectively (for IRAS 04407–7000, IRAS 04498–6842, IRAS 05003–6712 and IRAS 05558–7000 these values refer to the smoothed spectra shown in Figs. 1–4, with an effective channel width of  $0.36 \text{ km s}^{-1}$ ).

| Object name   | Integration time (s) | Velocity at peaks<br>(km s <sup>−1</sup> ) |          | $v_{\text{exp}}$<br>(km s <sup>−1</sup> ) | Peak flux density<br>(mJy) |        | $\sigma$<br>(mJy) | $F_{\text{int}}$<br>(mJy km s <sup>−1</sup> ) | $\sigma_{\text{int}}$<br>(mJy km s <sup>−1</sup> ) |
|---|----------------------|--|----------|---|----------------------------|--------|-------------------|---|--|
|   |                      | Blue                                       | Red      |   | Blue                       | Red    |                   |   |  |
| <i>LMC</i>  |                      |  |          |   |                            |        |                   |   |  |
| IRAS 04407–7000   | 33000                | 240  | 270?     | 15?                                       | 50                         | 8?     | 5.5               | 115   | 10   |
| IRAS 04498–6842   | 28800                | 246  | 272      | 13  | 23                         | 11     | 5.9               | 34  | 12   |
| IRAS 04553–6825   | 14455                | 252, 262                                   | 300, 280 | 24  | 600, 180                   | 70, 50 | 10.5              | 2,950   | 13   |
| IRAS 05003–6712   | 32010                | 268  |          |   | 33                         | ~13?   | 5.1               | 38  | 12   |
| IRAS 05558–7000   | 32500                | 265  | 285      | 10  | 17                         | 17     | 6.9               | 50  | 14   |
| <i>Sample from Wood et al. (1992) — excluding IRAS 04553–6825</i> |                      |  |          |   |                            |        |                   |   |  |
| IRAS 04545–7000   |                      | 258  | 274      | 8   | 140                        | 30     | 17                |   |  |
| IRAS 05280–6910   |                      | 255  | 289      | 17  | 90                         | 70     | 17                |   |  |
| IRAS 05298–6957   |                      | 271  | 292      | 10.5                                      | 240                        | 130    | 17                |   |  |
| IRAS 05329–6708   |                      | 301  | 323      | 11  | 70                         | 130    | 17                |   |  |
| IRAS 05402–6956   |                      | 263  | 284      | 10.5                                      | 80                         | 60     | 17                |   |  |

preparation for and based on *ISO* observations a considerable sample of these sources have now been classified according to their luminosity, variability, IR colours and chemical type (Zijlstra et al. 1996; van Loon et al. 1998a; Groenewegen & Blommaert 1998; Trams et al. 1999). As a result, we are able to select detectable OH/IR candidates with greater certainty. Their properties and those of previously detected magellanic OH/IR stars are listed in Table 1. We adopt a distance to the LMC of  $D_{\text{LMC}} = 50 \text{ kpc}$ , and a distance to the SMC of  $D_{\text{SMC}} = 60 \text{ kpc}$ .

The known OH maser sources all have extremely long pulsation periods ( $P \gtrsim 1200 \text{ d}$ ) and large pulsation amplitudes ( $\Delta K \gtrsim 1.5 \text{ mag}$ ) — except the very luminous red supergiant IRAS 04553–6825. They are all enshrouded in a thick dust envelope, making them red at short wavelengths ( $J - K \gtrsim 3 \text{ mag}$ ) and bright in the mid-IR ( $F_{25} \gtrsim 1 \text{ Jy}$ ). It has therefore been difficult to determine the optical spectral type for the OH/IR stars, but where it has been possible they were of late-M type. Their bolometric luminosities place them near or above the tip of the AGB ( $M_{\text{bol}} \simeq -7 \text{ mag}$ ). Hence targets were selected on the basis of being oxygen-rich and luminous, having red colours and bright mid-IR flux densities, and pulsating with very long periods and large amplitudes. In particular the knowledge of the chemical type has allowed us to avoid carbon stars — which do not exhibit OH maser emission (many of the Wood et al. (1992) targets have later been found to be carbon stars). Unfortunately, not many such OH/IR candidates are known in the SMC; presumably because the potential candidates turn into carbon stars in this metal-deficient environment.

### 3 OBSERVATIONS

The 64m radio telescope at Parkes, Australia, was used from 14 to 22 August, 2003, to observe the OH satellite line at 1612 MHz. The multibeam receiver was used in two orthogonal polarizations, each of 8 MHz bandwidth and sampled with 8192 channels yielding  $0.18 \text{ km s}^{-1} \text{ channel}^{-1}$ .

Most of the observations were performed in frequency

switching mode with a frequency throw of 0.5 MHz ( $93 \text{ km s}^{-1}$  at 1612 MHz), with integration times of 5 sec in between. Total integration times amounted to about 15,000 sec, and double that for objects that were re-observed to confirm a suspected detection. The first experiments on IRAS 04498–6842, IRAS 04509–6922 and IRAS 04553–6825 were performed in position switching mode, alternately observing the source and patches of (presumed empty) sky at  $30'$  to the North and South. Most of the integration time on these sources was however obtained in frequency switching mode. IRAS 04553–6825 was observed daily and also used for flux calibration checks.

The data were processed into blocks of 250 sec worth of raw data with the spectral line reduction programme SPC. Off-line reduction consisted of combining the spectra with the various polarizations and frequency settings, and baseline subtraction. A Fortran code was written to do this, but also to first clean the spectra from human-made interference which can generate strong spikes in the spectrum. These generally decay within a couple of integrations, but they may persist in the average spectrum and be confused as a genuine feature. There was a noticeable increase in the level of this “spikey” noise during daytime.

The code, NOSPIKE, works as follows: first a baseline is subtracted, using the mode of 50 channels at a time. Then the mode of the squared values is calculated to obtain a measure for the spread,  $\sigma$ , specifying a minimum value for  $\sigma$  to make it robust against anomalously low values in the presence of strong signal. The programme then runs through every data point and if a value is greater than a specified number of  $\sigma$ , that value is replaced with the preceding value. The same code then averages the polarizations and frequencies as appropriate (depending on the observing mode), and stacks the observations, weighted according to exposure time and the inverse square of system temperature (which was  $\sim 37 \text{ K}$  most of the time).

The method of combining the spectra that provided the best signal-to-noise ratio was the Total Power method, where the frequency-switched spectra were aligned and averaged rather than ratio-ed first. This therefore did not re-

**Table 3.** Non-detections, with values for the rms noise level in the original spectrum and that which is obtained for any emission integrated over a  $10 \text{ km s}^{-1}$  interval.

| Object name     | Integration time (s) | $\sigma$ (mJy) | $\sigma_{\text{int}}$ (mJy $\text{km s}^{-1}$ ) |
|-----------------|----------------------|----------------|---|
| <i>SMC</i>      |                      |                |   |
| IRAS 00483–7347 | 13000                | 9              | 27  |
| IRAS 00591–7307 | 17000                | 8              | 24  |
| <i>LMC</i>      |                      |                |   |
| IRAS 04509–6922 | 24660                | 17             | 63  |
| IRAS 04516–6902 | 15500                | 11             | 47  |
| IRAS 05294–7104 | 16000                | 13             | 42  |

move the baseline, which was done by subtracting a heavily smoothed version of the original spectrum. This method was not robust enough for IRAS 04553–6825 due to its extremely strong emission, and for this source the baseline was instead fitted with a low-order polynomial function. The spectra of the OH maser detections — except IRAS 04553–6825 — were smoothed by a factor two in order to reduce noise but preserve maser emission features.

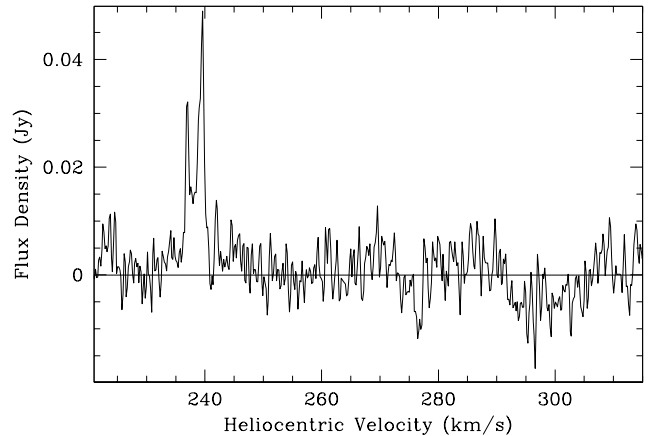
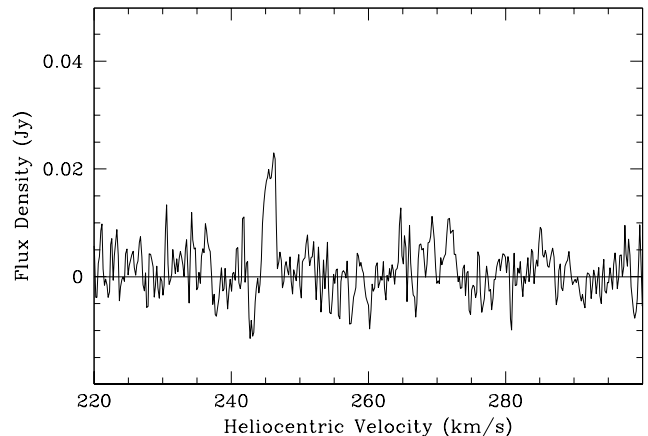
## 4 RESULTS

Tables 2 & 3 show the obtained results for the OH maser detections and non-detections, respectively. The wind speed  $v_{\text{exp}}$  is derived from the separation of the blue and red peaks<sup>1</sup>,  $\Delta v_{\text{blue-red}}$ , rather than from the separation of the extreme velocities where emission is detected (and which is very hard to determine in noisy spectra). The integrated flux is obtained by integrating over either the blue peak or the whole maser profile where the red component is clearly identified. Upper limits for the emission from the targets that failed to yield a clear maser detection may be taken to be  $3\sigma$ . The individual detections and the non-detections are described in separate subsections below.

The observed velocities of the bulk of the ISM seen in H I may in some cases support or challenge claims for detected maser emission, as the OH/IR stars are generally massive (hence young) enough to follow the kinematics of the ambient ISM from which they have formed. Van Loon et al. (2001b) demonstrated this to be the case for circumstellar masers in the LMC. Where we refer to the H I velocities we have inspected the Parkes 21 cm Multibeam Project<sup>2</sup> datacube along the lines-of-sight towards our targets. For a global overview of the structure and kinematics of the H I gas in the magellanic clouds the reader is referred to Kim et al. (1998; LMC) and Stanimirović et al. (1999; SMC).

### 4.1 IRAS 04407–7000

IRAS 04407–7000 is in all respects a typical massive dust-enshrouded tip-AGB star. An integration with the AT Compact Array at high spatial resolution led to the detection of

**Figure 1.** OH 1612 MHz maser emission from IRAS 04407–7000.**Figure 2.** OH 1612 MHz maser emission from IRAS 04498–6842.

a single-peaked 1612 MHz OH maser (van Loon et al. 1998a) at a heliocentric velocity of  $239 \text{ km s}^{-1}$ . The peak flux density was  $F_{\text{peak}} \sim 50 \text{ mJy}$ , at  $0.7 \text{ km s}^{-1} \text{ channel}^{-1}$  and an rms noise level of  $\sigma \sim 12 \text{ mJy}$ .

Our much deeper integration with Parkes confirms the presence of strong OH maser emission at  $240 \text{ km s}^{-1}$ , again peaking at  $F_{\text{peak}} \sim 50 \text{ mJy}$ , but also shows a secondary peak blueshifted by a few  $\text{km s}^{-1}$  (Fig. 1). This is probably substructure within one of the maser components — most likely the blue component (see Sect. 5). In one of the two observations for this source a complementary peak at  $270 \text{ km s}^{-1}$  was visible, which would result in a wind speed of  $15 \text{ km s}^{-1}$  (but we omit this estimate from further analysis). The H I data along this line-of-sight was heavily affected by emission in the sidelobes of the dish, which occurred at velocities around  $240$  to  $260 \text{ km s}^{-1}$ . If this is also representative for the neutral hydrogen near IRAS 04407–7000, then these velocities are consistent with our interpretation of the strong peak at  $240 \text{ km s}^{-1}$  being the blue component.

### 4.2 IRAS 04498–6842

IRAS 04498–6842 is very luminous, but its long pulsation period, large pulsation amplitude and fairly moderate mid-IR luminosity suggests it is an AGB star rather than a supergiant. The high luminosity might result from Hot Bottom

<sup>1</sup> We refer to the peak at the lowest heliocentric velocity as the “blue” peak and the higher velocity component as the “red” peak.

<sup>2</sup> <http://www.atnf.csiro.au/research/multibeam/>

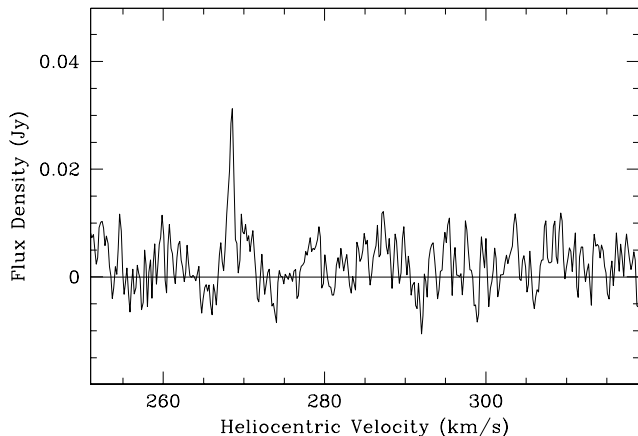


**Figure 3.** OH 1612 MHz maser emission from IRAS 05003–6712.

Burning — which also prevents AGB stars in the LMC that are more massive than  $\sim 4 M_{\odot}$  from becoming carbon stars (van Loon et al. 2001a). Or the bolometric luminosity calculated by Whitelock et al. (2003), which was based on the limited *IRAS* data, may be an overestimate of the true mean luminosity (indeed the luminosity determined from *ISO* observations is lower).

Its OH spectrum (Fig. 2) shows a rather blunt blue-shifted peak at  $246 \text{ km s}^{-1}$ , and a fainter red component at  $272 \text{ km s}^{-1}$ , which implies a wind velocity of  $13 \text{ km s}^{-1}$ . Although the red component is at the limit of the detection sensitivity, it was visible on both days on which IRAS 04498–6842 was observed. The H I emission peaks sharply at  $\sim 260 \text{ km s}^{-1}$ , which agrees very well with the velocities of the blue and red OH maser components in IRAS 04498–6842.

#### 4.3 IRAS 05003–6712

Although IRAS 05003–6712 is the faintest (bolometrically and at mid-IR wavelengths) object and has one of the shortest pulsation periods amongst the targets, it is still an extremely dust-enshrouded ( $J - K = 3 \text{ mag}$ ;  $F_{25} = 0.33 \text{ Jy}$ ), luminous ( $M_{\text{bol}} = -6.2 \text{ mag}$ ) and cool (spectral type M9) AGB star with strong ( $\Delta K = 1.6 \text{ mag}$ ) stellar pulsations. It is therefore not unexpected that we detected OH maser emission from this source (Fig. 3).

The OH spectrum (Fig. 3) shows a sharp blue-asymmetric<sup>3</sup> peak at  $268 \text{ km s}^{-1}$ , but it is not clear where would be the corresponding red component. The H I spectrum is affected by sidelobe interference around 260 to 280  $\text{km s}^{-1}$ , leaving emission from the main beam visible around 280 to 300  $\text{km s}^{-1}$ . This suggests indeed that the  $268 \text{ km s}^{-1}$  OH maser peak is the blue component.

#### 4.4 IRAS 05558–7000

IRAS 05558–7000 is a typical dust-enshrouded tip-AGB star. With  $J - K > 3 \text{ mag}$  it is also the reddest target,

<sup>3</sup> By “blue-asymmetric” we mean that the flux density at the short wavelength side of the centre of the line profile is higher than at the long wavelength side.

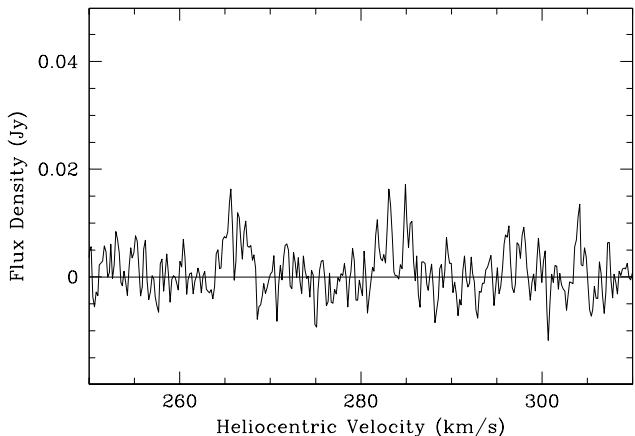


**Figure 4.** OH 1612 MHz maser emission from IRAS 05558–7000.

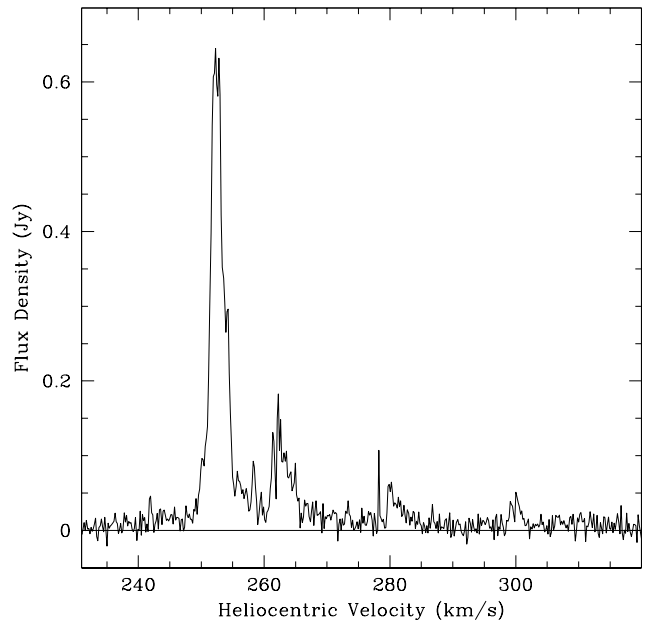


**Figure 5.** OH 1612 MHz maser emission from IRAS 04553–6825.

and its optical spectrum was too dim to classify (note however that at least four of the Wood et al. (1992) OH/IR stars are redder than IRAS 05558–7000).

The OH spectrum of this source (Fig. 4) is unusual within this sample as both the blue (at  $265 \text{ km s}^{-1}$ ) and red (at  $285 \text{ km s}^{-1}$ ) components are equally bright (17 mJy). Situated in the outskirts of the LMC, the H I emission (affected by sidelobe interference around 260 to 280  $\text{km s}^{-1}$ ) extends to at least  $350 \text{ km s}^{-1}$ , and is therefore of limited help in affirming the interpretation of the OH spectrum of IRAS 05558–7000.

#### 4.5 The red supergiant IRAS 04553–6825

The coolest, most luminous known LMC red supergiant, IRAS 04553–6825 has been much studied and was part of the sample observed by Wood et al. (1992). It has been found to have extremely strong maser emission from several

sources: OH (Wood, Bessel & Whiteoak 1986), H<sub>2</sub>O (van Loon et al. 1998b) and SiO (van Loon et al. 1996).

Detailed work on the H<sub>2</sub>O and SiO maser emission by van Loon et al. (2001b) indicated that the location of the star was at a greater velocity than suggested by Wood et al. (1992), whose observations it turned out had shown double-peaked structure within the blue-shifted component only. Our new data clearly reveals two components, at 280 and 300 km s<sup>-1</sup> (Fig. 5), which are red-shifted with respect to the previously detected OH maser emission as well as red-shifted with respect to the peaks in the SiO and H<sub>2</sub>O maser emission which indicate the systemic (stellar) velocity at  $v_* \sim 278$  km s<sup>-1</sup> (Fig. 6) — intriguingly, an extremely sharp OH emission spike was detected at exactly this systemic velocity. The systemic velocity is confirmed by the H I emission which peaks around  $\sim 270$  km s<sup>-1</sup>.

A possible explanation for the multiple maser emission components would be the presence of two expanding dust shells. The faster of these, with a wind speed of  $v_{\text{exp}} \sim 24$  km s<sup>-1</sup>, is kinematically quite symmetrical with respect to the systemic velocity. Similar OH maser profiles in other sources have also been interpreted as due to bipolar outflows (Chapman 1988). Over the two decades that have passed since the first spectrum, the blue-most peak has increased in strength whilst the secondary blue component (at 262 km s<sup>-1</sup>) has diminished in strength. This may reflect changes in the structure of the circumstellar matter distribution, but as maser emission is a highly non-linear process it is very sensitive to small changes in the conditions required for the population inversion and velocity coherency to occur.

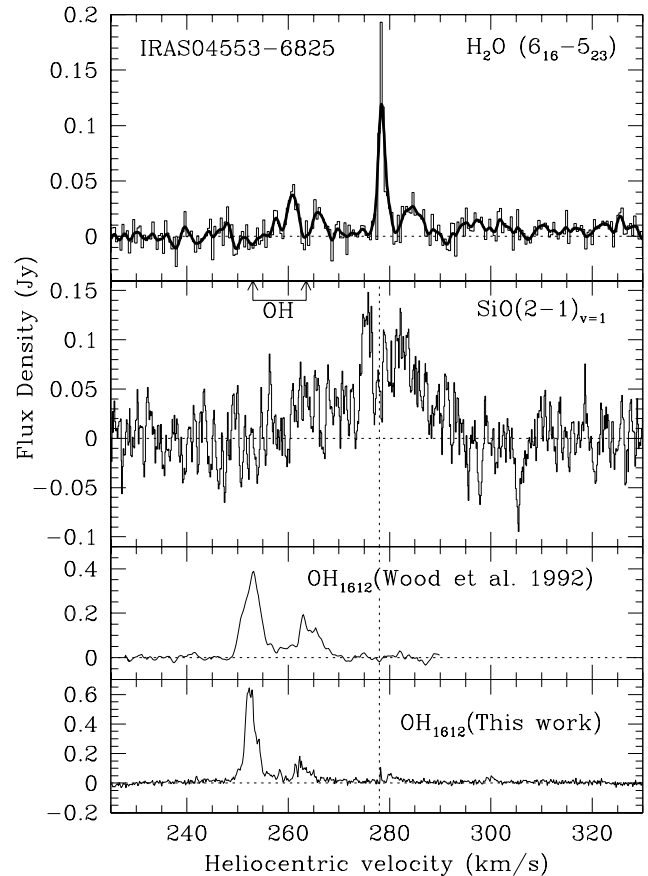


**Figure 6.** Comparison of the masers detected in IRAS 04553–6825 (after van Loon et al. 2001b).

#### 4.6 Non-detections

On the basis of the (circum)stellar parameters the remaining three targets IRAS 04509–6922, IRAS 04516–6902 and IRAS 05294–7104 could have been expected to exhibit OH maser emission at a similar level as the successfully detected (AGB) OH/IR stars in the LMC. However, stronger than average interference and time constraints resulted in rather noisy spectra (Fig. 7; for comparison, spectra smoothed by a factor 11 are offset by a small amount). Hints of emission features were not generally stable with time and are hence deemed spurious until confirmed. IRAS 04509–6922 was observed at a similar noise level by Wood et al. (1992), who also failed to detect OH maser emission in this source. The H I emission occurs at velocities in the range 260 to 280 km s<sup>-1</sup> for IRAS 04509–6922 and IRAS 04516–6902, and 220 to 270 km s<sup>-1</sup> for IRAS 05294–7104.

Because there was no clear indication of maser emission in either of the SMC targets after the first integrations, further effort was concentrated on the LMC sources. Hence no circumstellar OH masers were found in the SMC, although future observations might confirm potential emission between 130 and 150 km s<sup>-1</sup> in IRAS 00483–7347 (Fig. 8; the offset spectra are smoothed by a factor 11). The H I emission covers a much wider range in velocities than in the LMC, from about 100 to 190 km s<sup>-1</sup> in the direction of IRAS 00483–7347 and 120 to 200 km s<sup>-1</sup> in the direction of IRAS 00591–7307.

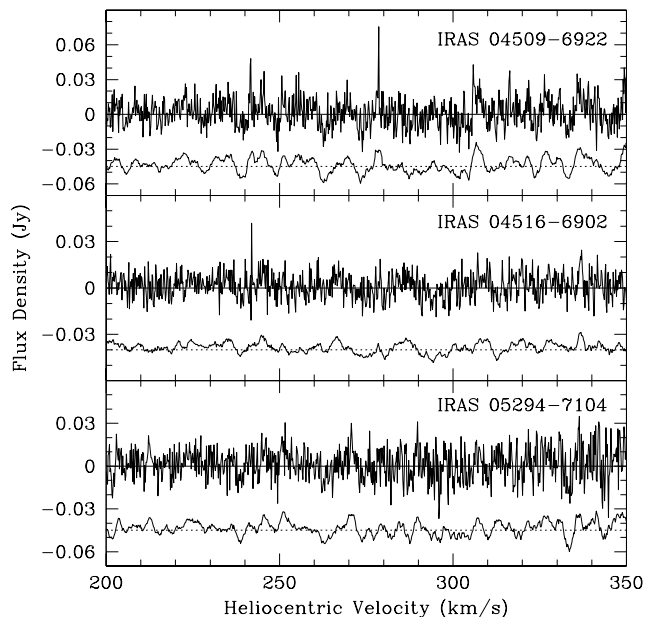


**Figure 7.** OH maser non-detections in three LMC targets.

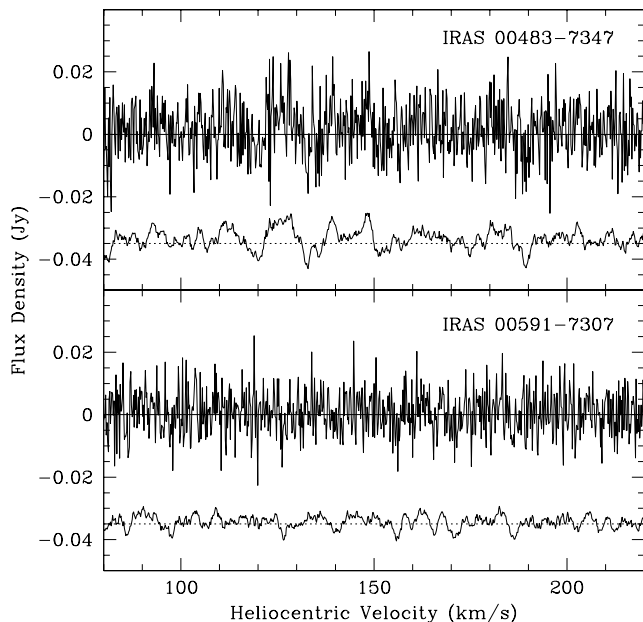


Figure 8. OH maser non-detections in two SMC targets.

## 5 DISCUSSION

### 5.1 Galactic comparison samples

#### 5.1.1 Galactic centre

The only reasonably homogeneous comparison sample of OH/IR stars at a known distance, the OH/IR stars in the galactic centre region of the Milky Way galaxy provide the best comparison for the enlarged sample of OH/IR stars in the LMC. The sample is described in Wood, Habing & McGregor (1998) who identified IR counterparts, and measured their bolometric luminosities and pulsation periods, of OH maser sources from the galactic centre surveys by Lindqvist et al. (1992) and Sjouwerman et al. (1998). We adopt a distance to the galactic centre of  $d_{GC} = 8$  kpc.

Blommaert et al. (1998), on the basis of similar data, argue for the presence of a metal-rich ( $\sim 3$  times solar) population of OH/IR stars with  $v_{exp} \gtrsim 18$  km s $^{-1}$ , and a somewhat less metal-rich and possibly older population of OH/IR stars with  $v_{exp} \lesssim 18$  km s $^{-1}$ , a conclusion that was supported by Wood et al. (1998). We note, however, that the galactic centre objects are significantly fainter and therefore probably have significantly lower initial masses than the LMC objects.

#### 5.1.2 Galactic disk

Galactic disk samples represent a mixture of stellar properties in between those of the Magellanic Cloud and galactic centre populations. Although this may lead to less ambiguous conclusions, it may also bridge the gap in parameter space between the fairly massive metal-poor OH/IR stars in the LMC and the less-massive metal-rich OH/IR stars in the galactic centre.

We here compare with two galactic disk samples: (i) te Lintel Hekkert et al. (1991), and (ii) Groenewegen et al. (1998, their Appendix B). The Groenewegen et al. sample also contains information about the pulsation periods, but

the te Lintel Hekkert et al. sample contains more OH masers. There is real overlap between sources in these two samples, and both samples can be considered equally representative of the galactic disk population of OH/IR stars, with a natural bias towards sources that lie within the solar circle.

### 5.2 Blue-red asymmetry

Within our sample of LMC OH/IR stars, where both blue and red peaks are detected, the blue peak is usually stronger than the red peak — exceptions to this are IRAS 05329–6708 from Wood et al. (1992) which has a red peak that is stronger than the blue, and IRAS 05558–7000 where both peaks are of equal strength. This was also noted in van Loon et al. (2001b), who proposed that the blue peak might include a contribution from amplified stellar light in addition to the amplified circumstellar radiation (Fig. 9). Indeed, VLBI observations of nearby, galactic OH and H<sub>2</sub>O masers indicate the possibility for maser amplification of radiation originating from the stellar radiosphere (Vlemmings, van Langevelde & Diamond 2002; Vlemmings et al. 2003).

This predominant blue-asymmetry of the OH maser peaks in the LMC objects is in stark contrast to the rather even distribution of blue/red peak flux density ratios found in the galactic centre OH/IR stars (Fig. 10). There may be a dependence on the bolometric luminosity, with the most blue-asymmetric profile found in the by far most luminous object (IRAS 04553–6825). Two effects may be at work here: (i) the LMC objects are more luminous than the galactic centre objects, which means that any contribution from amplified stellar light is expected to be greater in the LMC objects, and (ii) the lower metallicity — and hence lower dust-to-gas ratio — in the LMC objects may cause the contribution from amplified circumstellar radiation to be smaller than in the galactic centre objects.

Competition between radiation which propagates outwards through the circumstellar envelope and that which propagates inwards may enhance the blue-asymmetry in the observed OH maser profile if the outwards propagating maser utilises most of the population-inverted OH molecules, leaving little for the inwards propagating maser. This would further diminish the red maser component which results from inwards travelling radiation through the receding part of the circumstellar envelope. Another consequence of this mechanism would be that the amplification of the red maser component becomes less radially beamed. This increased isotropy further diminishes the strength of the observed maser radiation and might lead to underestimation of the wind speed as inhomogeneities in the outflow yield similarly faint maser spots at a variety of projected radial velocities.

Our findings are corroborated by data on galactic disk OH masers (Fig. 11). The most red-asymmetric OH maser profiles have a ratio of blue and red OH maser peak flux density of no less than 1:6. However, there are several examples of OH maser profiles with this ratio in excess of 6:1. This suggests that extremely blue-asymmetric profiles are not merely the tail of an otherwise symmetric distribution of blue over red peak flux density ratios. On average the wind speeds of these extremely blue-asymmetric OH masers are indistinguishable from the bulk of the OH masers, although there is a conspicuous lack of such sources with wind speeds

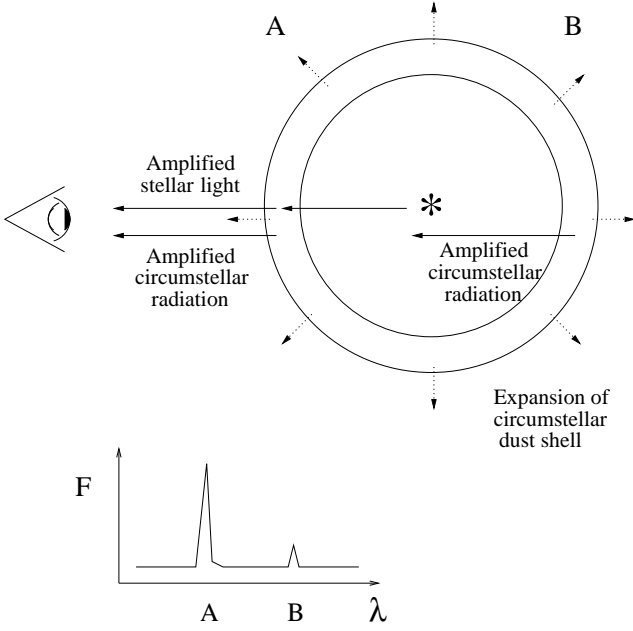


**Figure 9.** Explanation for the blue asymmetry of the OH maser profile as due to the contribution from amplified stellar radiation. Shown are the maser components which contribute to the observed spectrum.

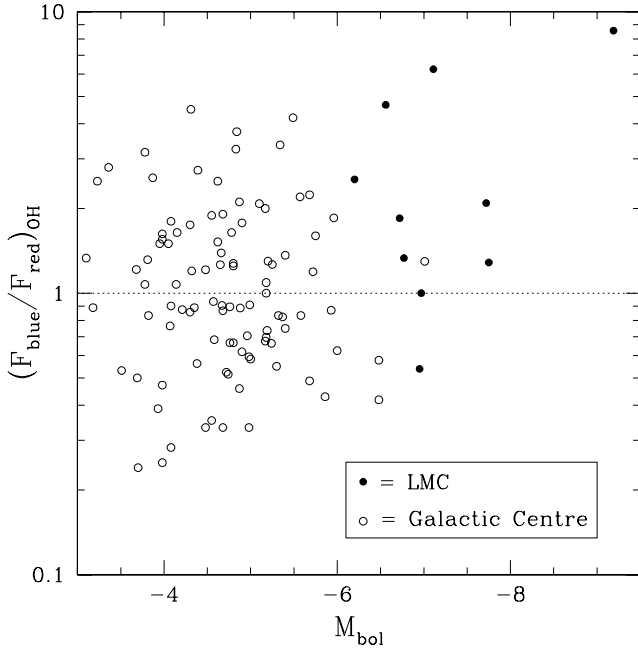


**Figure 10.** The ratio of the blue and red OH maser peak flux densities, versus bolometric luminosity, for OH/IR stars in the LMC (dots) and galactic centre (circles).

below  $10 \text{ km s}^{-1}$  (Fig. 11, top panel). They are, however, significantly brighter (on average) OH masers than the bulk (Fig. 11, centre panel). Their exclusively low galactic latitudes,  $|b_{\text{II}}| < 5^\circ$  (Fig. 11, bottom panel), strongly suggest that these extreme OH masers are also more distant and hence more luminous in an absolute sense.

OH/IR stars with the fastest winds,  $v_{\text{exp}} > 22 \text{ km s}^{-1}$

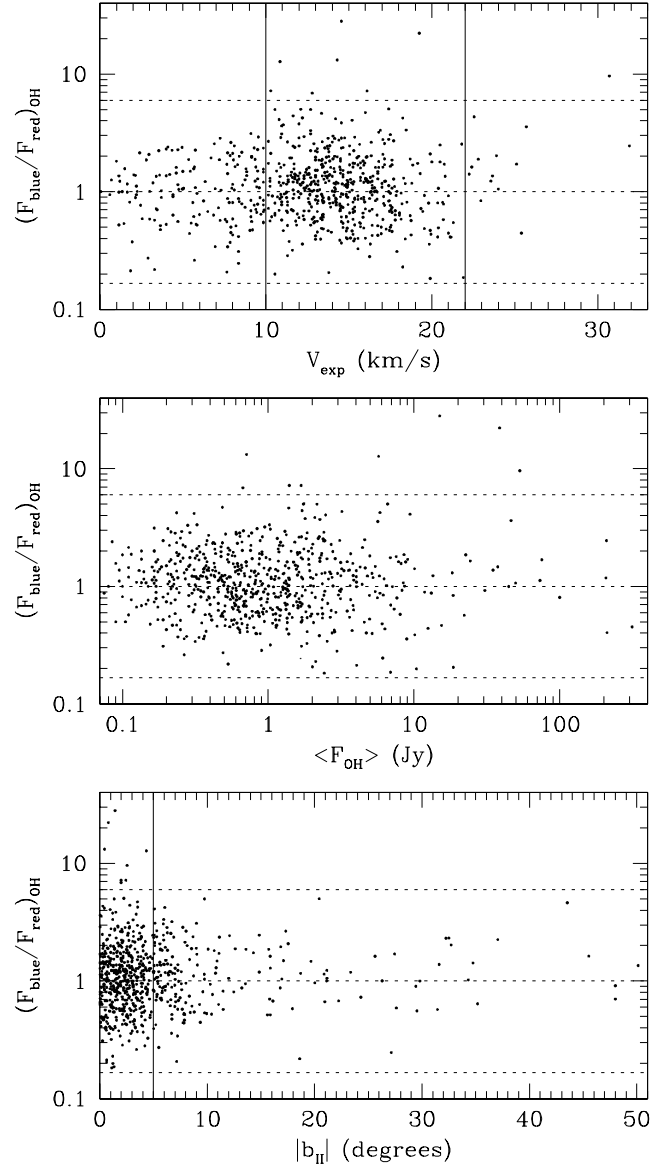


**Figure 11.** The ratio of the blue and red OH maser peak flux densities, versus wind speed (top), mean OH maser peak flux (centre) and galactic latitude (bottom), for OH/IR stars in the galactic disk (te Lintel Hekkert et al. 1991). The dotted horizontal lines are for symmetric OH maser profiles and for ratios of the blue and red OH maser peak flux densities of 6:1 and 1:6, respectively. See text for an explanation of the vertical lines in the top and bottom panels.

(Fig. 11, top panel), are predominantly blue-asymmetric, in particular the two objects with  $v_{\text{exp}} > 30 \text{ km s}^{-1}$ . Such fast winds are most likely due to the high luminosity of the central star. Indeed, some of the best-studied red supergiants, NML Cyg, VY CMa, VX Sgr, S Per and IRC+10420 have fast outflows,  $v_{\text{exp}} \sim 20$  to  $30 \text{ km s}^{-1}$ , and they all have blue-asymmetric profiles of 1612 MHz OH maser emission (Cohen et al. 1987; Richards et al. 1999). A similar situation may occur in post-AGB objects where a central source of radio emission in the form of an ionized wind may dominate the maser amplification over the fainting, detached circumstellar dust envelope itself (Zijlstra et al. 2001).

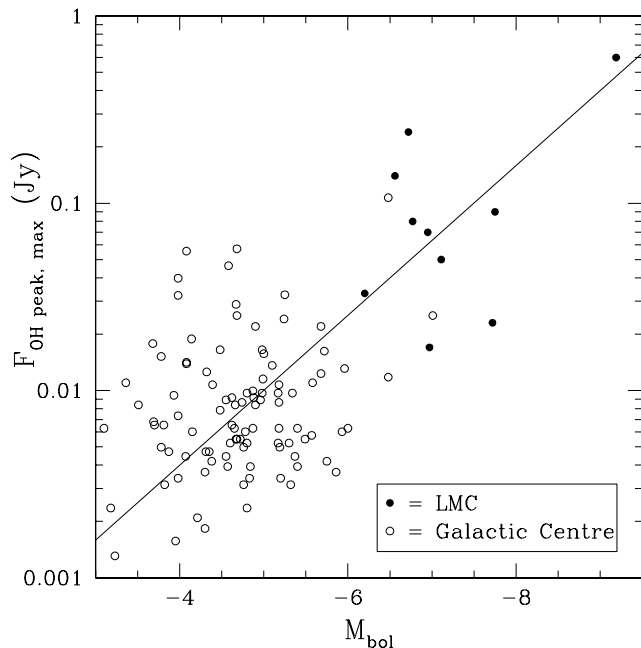


**Figure 12.** OH peak flux density versus bolometric luminosity, for OH/IR stars in the LMC (dots) and galactic centre (circles). The straight line corresponds to  $F_{\text{OH peak, max}} \propto L$ .

### 5.3 OH maser strength

In a lower metallicity environment the interstellar radiation field is stronger and penetrates deeper into the circumstellar envelope (Lequeux et al. 1994), which may lead to more dissociation of  $\text{H}_2\text{O}$  into OH. However, at lower metallicity the abundance of  $\text{H}_2\text{O}$  in the circumstellar envelope may be lower, resulting in a lower OH abundance. Do these effects cancel?

When plotted against bolometric magnitude (Fig. 12) the OH maser peak flux densities of the LMC sample seem to follow from a direct scaling of the galactic centre sample. This might be reconciled with similar OH abundances in both populations of objects, where the difference in OH maser strength is only due to a difference in the amount of radiation supplied by the embedded star (either directly or via re-emission by the circumstellar dust). This may seem remarkable given the fact that the abundance of the OH molecule also depends on the mass-loss rate, which is shown to depend on luminosity (van Loon et al. 1999) — but perhaps not on metallicity (van Loon 2000). However, if the masers are saturated then the rate at which 1612 MHz OH photons are emitted is expected to be proportional to the pumping photon flux and hence (see below) the infrared flux, which is the bolometric luminosity for an optically thick envelope. In this case the metallicity does not matter.

The OH maser pump efficiency may be expressed as the ratio of the OH maser peak flux density over the flux density of the 35  $\mu\text{m}$  OH line. This line is believed to be responsible (in part) for establishing the population inversion in the OH molecule which allows for the maser mechanism to operate (Elitzur et al. 1976). In the absence of direct measurements for the 35  $\mu\text{m}$  flux density the *IRAS* 25  $\mu\text{m}$  flux density is taken instead. For OH/IR stars in the galactic disk this leads to efficiencies in the region of  $\langle F \rangle / F_{25} \sim 1\%$  to  $\sim 20\%$ .

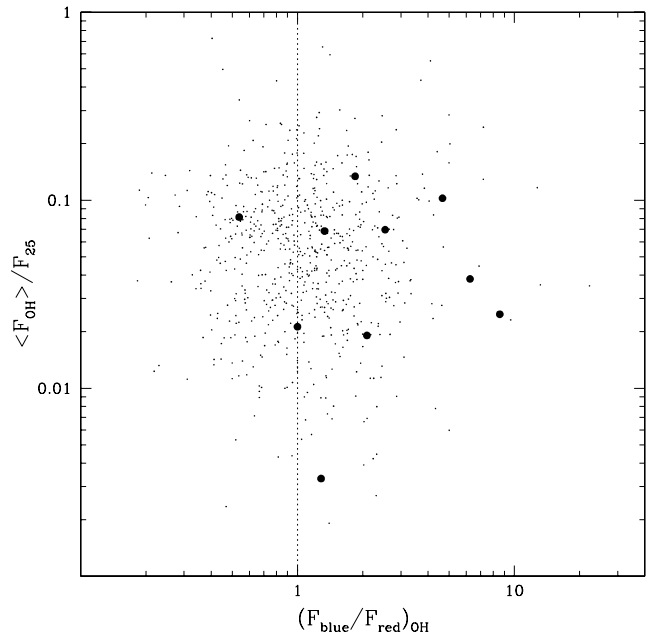


**Figure 13.** OH maser pump efficiency expressed as the ratio of mean OH maser peak flux density over *IRAS* 25  $\mu\text{m}$  flux density, versus the ratio of the blue and red OH maser peak flux densities, for OH/IR stars in the LMC (circles) and galactic disk (dots; te Lintel Hekkert et al. 1991). The dotted vertical line is for symmetric OH maser profiles.

With efficiencies of  $\langle F \rangle / F_{25} \sim 6 \pm 4\%$  the LMC sources (Fig. 13, circles) are indistinguishable from galactic disk objects (Fig. 13, dots). There is no indication for the efficiency to be higher (or lower) in sources of blue-asymmetric OH maser profiles. This suggests that the 1612 MHz OH masers in both the galactic and LMC objects are indeed saturated.

A significant contribution to the scatter observed in Figs. 10 & 12 is due to variability, both in bolometric luminosity and OH maser intensity. Whitelock et al. (2003) and Wood et al. (1992, 1998) derived time-averaged bolometric magnitudes on the basis of near-IR photometric monitoring data, but for the most extremely dust-enshrouded sources a significant fraction of the total luminosity emerges at mid-IR wavelengths at which no such monitoring data is available. The values for  $M_{\text{bol}}$  may thus be uncertain by up to a few tenths of a magnitude, but this is accurate enough for the purpose of the analyses performed here. The OH maser spectra were generally obtained only once per object. The peak intensity of OH masers is known to vary by typically a factor two (Herman & Habing 1985; van Langevelde et al. 1993) and, whilst contributing to the observed scatter, will not inhibit the detection of trends or a statistical comparison between the magellanic and galactic samples.

### 5.4 Mass-loss rates from OH maser intensities

If the OH maser is saturated then the peak flux density depends on the number of population-inverted OH molecules, and may thus be a measure of the mass-loss rate. Baud & Habing (1983) proposed a prescription for this, based on a calibration against OH/IR stars in the galactic disk. We use their prescription to predict the mass-loss rates for OH/IR

stars in the LMC, in a form presented by van der Veen & Rugers (1989):

$$\dot{M} = 1.8 \times 10^{-7} \sqrt{F_{\text{OH}}} v_{\text{exp}} D, \quad (2)$$

where  $\dot{M}$  is the mass-loss rate in  $M_{\odot} \text{ yr}^{-1}$ ,  $F_{\text{OH}}$  is the OH 1612 MHz maser peak intensity in Jy,  $v_{\text{exp}}$  is the wind speed in  $\text{km s}^{-1}$  and  $D$  is the distance in kpc (Fig. 14, dotted line). These predictions can be compared with the mass-loss rates as obtained from modeling of the spectral energy distributions by van Loon et al (1999) (Fig. 14, points). The predicted mass-loss rates are clearly too low, but they can be brought in line with the measured mass-loss rates by reducing the OH abundance by a factor 5 (Fig. 14, solid line) — in Eq. (2) the OH abundance was assumed to be  $f_{\text{OH}} = 1.6 \times 10^{-4}$  (see Goldreich & Scoville 1976). This would suggest that the dominant factor in determining the OH abundance in the superwind of OH/IR stars is the oxygen abundance (i.e. metallicity), rather than the strength of the interstellar radiation field to dissociate  $\text{H}_2\text{O}$ .

Zijlstra et al. (1996), based on a comparison with mass-loss rates as derived from the IR dust emission, proposed an alternative prescription for the *dust* mass-loss rate:

$$\dot{M}_{\text{dust}} = 1.6 \times 10^{-10} F_{\text{OH}} v_{\text{exp}} D^2. \quad (3)$$

The rationale behind this recipe is that if the OH maser is saturated then the maser flux depends on the IR flux which pumps the population inversion, and the OH maser is thus a measure of the dust mass-loss rate. Its predictions for the LMC (Fig. 15, dotted line) fall below the measured values (Fig. 15, points) by a factor 2, which may be accounted for by systematic uncertainties in the modeling of the IR emission — both for the LMC objects as well as the galactic data that was used to calibrate Eq. (3).

The LMC data obey a relation of the type  $\dot{M} \propto F_{\text{OH}}$  (Eq. (3), Fig. 15) better than one of the type  $\dot{M} \propto \sqrt{F_{\text{OH}}}$  (Eq. (2), Fig. 14). This is unfortunate as it deprives us from a means to measure the gas mass-loss rate if the OH maser emission yields the dust mass-loss rate instead.

### 5.5 The wind speed

We find a spread in wind speed comparable to that found in the galactic centre (Figs. 16 & 17). In general, higher velocities are found associated with the most luminous stars (Fig. 14). It is clear, however, that at the same luminosity, stars in the LMC have a lower wind speed. We can reproduce these trends with Eq. (1), which is consistent for dust-to-gas ratios  $\Psi_{\text{GC}}/\Psi_{\text{LMC}} \simeq 6.5$  (dotted sequences in Fig. 16). This is very similar to the ratio of the metallicities of the metal-rich galactic centre sample and metal-poor LMC sample.

Most of the OH/IR stars in the galactic centre sample have shorter pulsation periods than those in the LMC (Fig. 17). The difference in speed is smaller between stars of comparable period than that shown in Fig. 16. In particular, the OH/IR stars with the longest pulsation periods do not generally have the fastest winds. This may be related to the changes in the stellar structure as a result of the mass lost. It is important to bear in mind, though, that the samples differ on at least one more crucial point: their progenitor masses. Indeed, on average, at similar pulsation periods the wind speeds of the Groenewegen et al. galactic disk sample

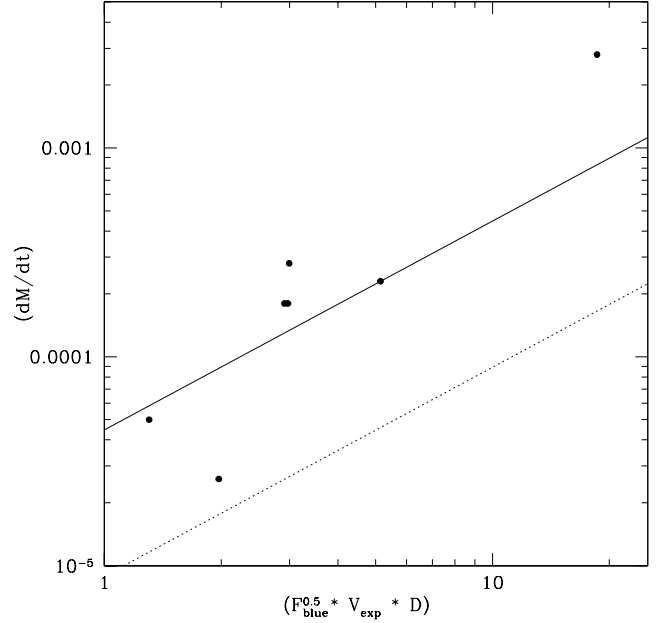


**Figure 14.** Predicted mass-loss rates following the Baud & Habing (1983) recipe (Eq. (2), dotted line) and LMC data with mass-loss rates from van Loon et al. (1999) (points). The predictions can be scaled up to globally fit the data (but not the slope) by reducing the OH abundance by a factor 5 (solid line).

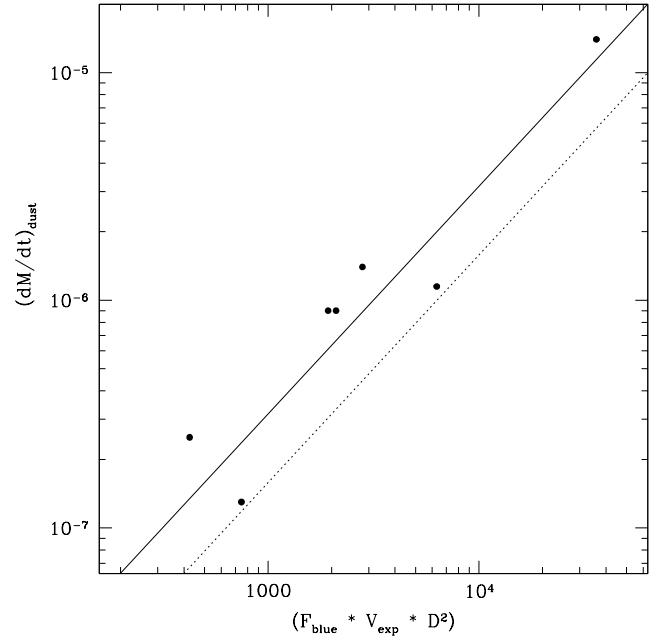


**Figure 15.** Predicted dust mass-loss rates following the Zijlstra et al. (1996) recipe (Eq. (3), dotted line) and LMC data with mass-loss rates from van Loon et al. (1999) (points). The predictions can be scaled up by a factor 2 to fit the data (solid line).

are intermediate between the Magellanic Cloud and galactic centre stars.

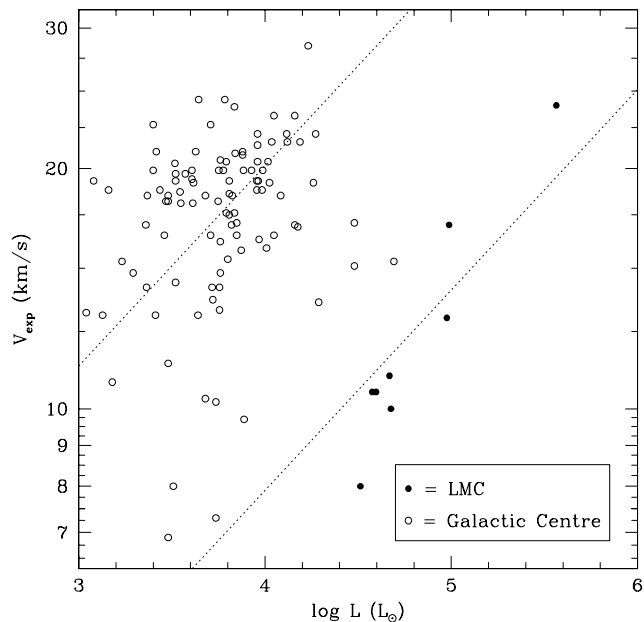


**Figure 16.** Wind speed versus bolometric luminosity, for OH/IR stars in the LMC (dots) and galactic centre (circles). The dotted sequences follow Eq. (1) for  $\Psi_{GC}/\Psi_{LMC} \simeq 6.5$ .

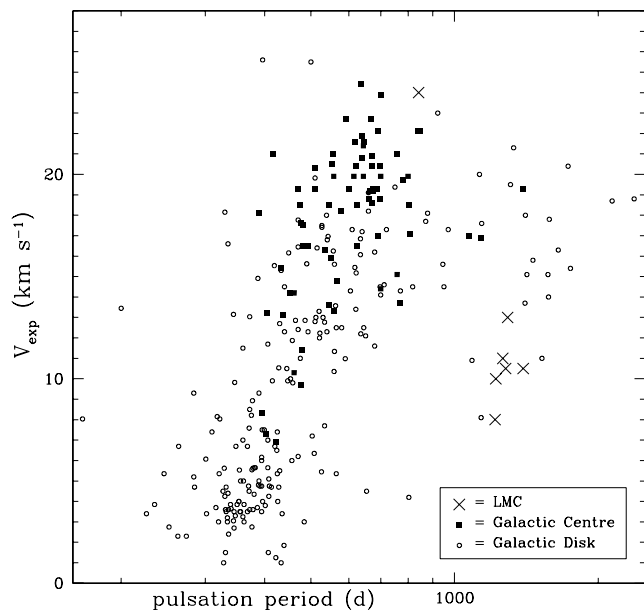


**Figure 17.** Wind speed versus period (after van Loon 2000), for OH/IR stars in the LMC (crosses), galactic centre (filled squares) and galactic disk (circles; Groenewegen et al. 1998).

## 5.6 Comparison of wind speed and escape velocity

We now compare the wind speed with the escape velocity from the “surface” of the star, from the dust formation zone and from further out in the wind where the OH masers originate. The stellar radius,  $R_*$ , is determined from the effective temperature,  $T_{\text{eff}}$  (estimated from the optical spectrum), and the luminosity,  $L$  (from  $M_{\text{bol}}$ ). The radius of the dust formation zone,  $R_{\text{dust}}$ , was obtained from detailed modelling

of the spectral energy distribution by van Loon et al. (1999). For the fully developed wind we adopt  $R_{\text{wind}} = 5 \times R_{\text{dust}}$ .

The masses of these objects are uncertain. However, we can assume masses of 4 to 8  $M_{\odot}$  as lower-mass objects would have become carbon stars and 8  $M_{\odot}$  corresponds to the upper limit for AGB evolution. IRAS 04553–6825 is a supergiant and will therefore be more massive ( $\sim 15$  to 50  $M_{\odot}$ ). IRAS 05280–6910 is in the  $\sim 10^7$ -year old cluster NGC 1984 and will have had a mass of  $\sim 15 M_{\odot}$  (Wood et al. 1992). IRAS 05298–6957 is also in a (small) cluster, HS 327, and had a mass of  $\sim 4 M_{\odot}$  (van Loon et al. 2001a). The masses for the other objects have been estimated on the basis of their luminosity. The adopted and calculated values for the masses, radii and escape velocities are listed in Table 4.

It is interesting to note that the escape velocity at the stellar surface is with  $v_{\text{esc},*} \simeq 43$  to 48  $\text{km s}^{-1}$  very similar for all tip-AGB stars. The escape velocities for the supergiants IRAS 04553–6825 ( $v_{\text{esc},*} = 71 \text{ km s}^{-1}$ ) and IRAS 05280–6910 ( $v_{\text{esc},*} \sim 67 \text{ km s}^{-1}$ ) are also very similar but significantly faster than those of the AGB stars. The galactic centre stars are almost certainly of significantly lower mass, and although their optical spectral types are not known there is no reason to believe that they should be on average warmer than M8. It is therefore very probable that the escape velocity at their stellar surface (here estimated as 36  $\text{km s}^{-1}$ ) is indeed lower than for the magellanic AGB stars of our sample.

At the speed as measured from the OH maser, the material would not have escaped from the stellar surface nor from the dust formation radius — except for the extremely luminous supergiant IRAS 04553–6825 — without further driving (Fig. 18). Netzer & Knapp (1987) show that the location of a maser of molecules produced by photodissociation (e.g. OH) is  $R_{\text{OH}} > 2R_{\text{dust}}$ . At this distance, the wind speed does exceed the local escape velocity for all OH/IR stars in the LMC (Fig. 18, dotted lines). Remarkably, this critical point seems to be very nearly identical for all OH/IR stars, at an “escape radius”  $R_{\text{esc}} \simeq 20,000 \times R_{\odot}$ , despite their differences in dust formation radii and hence acceleration timescales before reaching the escape radius. This scale may thus be fundamental to driving a steady outflow, and might result from the self-regulatory nature of dust-driven winds (Struck et al. 2004).

The galactic centre stars have with an average wind speed of 16.7  $\text{km s}^{-1}$  a relatively fast wind, which in combination with their low escape velocities results in a smaller escape radius of  $R_{\text{esc}} \sim 1,400 R_{\odot}$ . As the escape radius is similar for magellanic objects of vastly different masses (and luminosities), the most obvious stellar parameter that could be responsible for the differences between the escape radii in the LMC and the galactic centre is the metallicity.

We note that the current masses of the OH/IR stars are less than their progenitor masses due to the intense mass loss that made them OH/IR objects in the first place. Although the 12 and 25  $\mu\text{m}$  emission which led *IRAS* to detect the LMC sources is very bright, it originates from warm dust which was lost recently. Even the OH maser emission arises predominantly from material which was ejected  $t \sim 10^3$  yr ago (see van der Veen & Rugers 1989). At a steady mass-loss rate of  $\dot{M} \sim 10^{-5} M_{\odot} \text{ yr}^{-1}$ , this amounts to an ejected mass only of the order  $\Delta M \sim 0.01 M_{\odot}$ . If, however, the OH/IR phase of evolution is where these stars lose most

**Table 4.** Estimates for stellar mass and radius (see text), and the escape velocities at the stellar surface, at the dust formation zone (van Loon et al. 1999) and at a distance  $5\times$  as far. The wind speed is compared with these local escape velocities.

| IRAS                                     | $M$             | $L$                  | $T_{\text{eff}}$  | $R_{\star}$          | $R_{\text{dust}}$    | $v_{\text{esc}}$ (km s $^{-1}$ ) |                     |                             | $v_{\text{exp}}/v_{\text{esc}}$ |                     |                             |
|--|-----------------|----------------------|-------------------|----------------------|----------------------|----------------------------------|---------------------|-----------------------------|---------------------------------|---------------------|-----------------------------|
|  |                 |                      |                   |                      |                      | $[R_{\star}]$                    | $[R_{\text{dust}}]$ | $[5\times R_{\text{dust}}]$ | $[R_{\star}]$                   | $[R_{\text{dust}}]$ | $[5\times R_{\text{dust}}]$ |
| name                                     | ( $M_{\odot}$ ) | ( $10^3 L_{\odot}$ ) | (K)               | ( $10^3 R_{\odot}$ ) | ( $10^3 R_{\odot}$ ) |                                  |                     |                             |                                 |                     |                             |
| 04407–7000                               | 6               | 55                   | 3008              | 0.87                 | 7.7                  | 51.4                             | 17.2                | 7.7                         |                                 |                     |                             |
| 04498–6842                               | 8               | 97                   | 2500              | 1.66                 | 14.8                 | 42.8                             | 14.4                | 6.4                         | 0.30                            | 0.91                | 2.02                        |
| 04509–6922                               | 7               | 65                   | 2500              | 1.36                 | 8.1                  | 44.3                             | 18.1                | 8.1                         |                                 |                     |                             |
| 04516–6902                               | 6               | 55                   | 2667              | 1.10                 | 7.7                  | 45.5                             | 17.2                | 7.7                         |                                 |                     |                             |
| 04545–7000                               | 4               | 33                   | 2890 <sup>1</sup> | 0.73                 | 8.8                  | 45.7                             | 13.2                | 5.9                         | 0.18                            | 0.61                | 1.36                        |
| 04553–6825                               | 30              | 377                  | 3008              | 2.26                 | 36.2                 | 71.2                             | 17.8                | 8.0                         | 0.34                            | 1.35                | 3.02                        |
| 05003–6712                               | 4               | 24                   | 2667              | 0.73                 | 6.9                  | 45.9                             | 14.9                | 6.7                         |                                 |                     |                             |
| 05280–6910                               | 15              | 100                  | 2890 <sup>1</sup> | 1.26                 | 17.7 <sup>2</sup>    | 67.3                             | 18.0                | 8.0                         | 0.25                            | 0.95                | 2.11                        |
| 05294–7104                               | 5               | 41                   | 2890              | 0.81                 | 8.0                  | 48.5                             | 15.4                | 6.9                         |                                 |                     |                             |
| 05298–6957                               | 4               | 39                   | 2890 <sup>1</sup> | 0.79                 | 9.8                  | 44.1                             | 12.7                | 5.6                         | 0.24                            | 0.84                | 1.88                        |
| 05329–6708                               | 5               | 48                   | 2890 <sup>1</sup> | 0.87                 | 10.5                 | 46.7                             | 13.5                | 6.0                         | 0.24                            | 0.82                | 1.82                        |
| 05402–6956                               | 5               | 41                   | 2890 <sup>1</sup> | 0.80                 | 9.4                  | 48.7                             | 14.2                | 6.4                         | 0.22                            | 0.74                | 1.65                        |
| 05558–7000                               | 5               | 49                   | 2890 <sup>1</sup> | 0.88                 | 8.9                  | 46.5                             | 14.6                | 6.5                         | 0.22                            | 0.69                | 1.53                        |
| <i>Galactic centre comparison sample</i> |                 |                      |                   |                      |                      |                                  |                     |                             |                                 |                     |                             |
| Average                                  | 1               | 5.2                  | 2890 <sup>1</sup> | 0.29                 |                      | 36.3                             |                     |                             | 0.46                            |                     |                             |

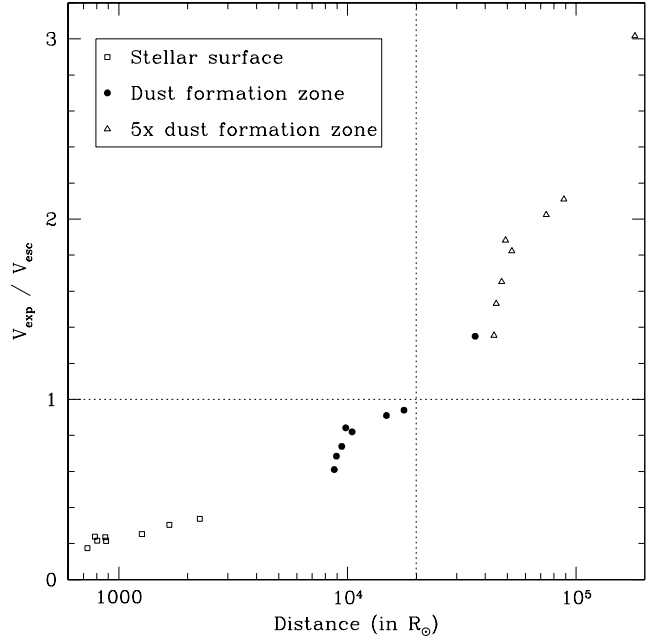
Notes: <sup>1</sup> adopted spectral type M8; <sup>2</sup> adopted  $R_{\text{dust}} = 14\times R_{\star}$ .

of their mass then statistically we can expect a (relatively massive) OH/IR star to have lost on average  $\sim 40\%$  of their progenitor mass. This would reduce our estimates for their escape velocities by a factor  $\sim \sqrt{0.6}$  and increase the ratios of  $v_{\text{exp}}/v_{\text{esc}}$  by the same factor  $\sim 1.3$  at all radii. Thus the stellar wind may in fact already have reached the escape velocity very near the dust formation zone (see Fig. 18). The reduced masses would lead to a reduction in the value for the escape radius for LMC stars to  $R_{\text{esc}} \simeq 10,000\times R_{\odot}$ . However, statistically an identical reduction would apply to all LMC stars, which would therefore still share a surprisingly common value for this lengthscale and one that is still significantly longer than for galactic centre stars.

## 6 CONCLUSIONS

We have presented the results of a new survey for OH maser emission at 1612 MHz in the circumstellar environments of magellanic dust-enshrouded giants.

Of the eight LMC sources selected, five were found to have OH masers, with at least one of the non-detections indicating that a detection is possible with increased integration time. This suggests that the sample was well chosen, due to the selection criteria employed: long pulsation period ( $P \gtrsim 800$  d), large pulsation amplitude ( $\Delta K \gtrsim 1.2$  mag), late oxygen-rich spectral type ( $\gtrsim \text{M8}$ ), red ( $J - K \gtrsim 2$  mag), and bolometrically and mid-IR bright ( $M_{\text{bol}} \lesssim -6$  mag and  $F_{25} \gtrsim 0.3$  Jy, respectively). We can thus be confident in our selection of future potential OH/IR stars. The strength of the OH maser peak in the LMC detections can be readily scaled from the strength of the OH maser peak in galactic centre sources on the basis of the differences in bolometric luminosity alone, without the need for an additional scaling due to the difference in metallicity. This provides some comfort for future searches for OH masers in the SMC or other low-metallicity environments.

**Figure 18.** Ratio of measured wind speed and estimated local escape velocity, versus the distance from the central star at which the escape velocity was evaluated.

The LMC sources show a pronounced asymmetry between the strength of the blue and redshifted emission, much more so than OH/IR stars in the galactic centre. We propose that this is due to a greater contribution of amplified radiation originating from the star itself, both in an absolute sense (bolometrically brighter stars) and because the lower metallicity of sources in the LMC leads to a smaller contribution of (amplified) circumstellar emission compared with OH/IR stars in the galactic centre.

Of the recipes for deriving mass-loss rates from the OH

maser emission from Baud & Habing (1983) for the gas mass-loss rate and from Zijlstra et al. (1996) for the dust mass-loss rate the LMC data follow the Zijlstra et al. predictions better than the Baud & Habing predictions. This supports the interpretation of Zijlstra et al. that the OH maser strength is a measure of the IR pumping flux and thus of the dust mass-loss rate.

We find that at the same luminosity or pulsation period, the difference in wind speed,  $v_{\text{exp}}$ , can be fully accounted for by metallicity effects. This agrees with the suggestion by Wood et al. (1998) that the stars with higher  $v_{\text{exp}}$  have higher metallicity. In addition, we show that the current observations are consistent with simple radiation-driven wind theory in which the wind speed depends on luminosity,  $L$ , and metallicity,  $z$ , as  $v_{\text{exp}} \propto z^{1/2} L^{1/4}$ .

We compare the wind speed with the escape velocities, evaluated at the stellar surface, in the dust formation zone and further out in the wind. We find that the wind speed exceeds the local escape velocity at an “escape radius” of about  $1\text{--}2 \times 10^4 R_{\odot}$  from the star (just beyond the dust condensation radius) — a value which is surprisingly similar for all OH/IR stars in the LMC, AGB stars and red supergiants alike (but different for galactic centre OH/IR stars).

## ACKNOWLEDGMENTS

We thank the staff at Parkes Observatory for their support and hospitality, and Mark Calabretta for correspondence regarding SPC. An anonymous referee is thanked for her/his constructive and useful comments. JRM is supported by a PPARC studentship, and MM is supported by a PPARC Rolling Grant.

## REFERENCES

- Baud B., Habing H.J. 1983, A&A 127, 73
- Blommaert J.A.D.L., van der Veen W.E.C.J., van Langevelde H.J., Habing H.J., Sjouwerman L.O. 1998, A&A 329, 991
- Chapman J.M. 1988, MNRAS 230, 415
- Cohen R.J., Downs G., Emerson R., et al. 1987, MNRAS 225, 491
- Elias J.H., Frogel J.A., Humphreys R.M. 1980, ApJ 242, L13
- Elias J.H., Frogel J.A., Humphreys R.M. 1985, ApJS 57, 91
- Elitzur M., Ivezić Ž. 2001, MNRAS 327, 403
- Elitzur M., Goldreich P., Scoville N. 1976, ApJ 205, 384
- Goldreich P., Scoville N. 1976, ApJ 205, 144
- Groenewegen M.A.T., Blommaert J.A.D.L. 1998, A&A 332, 25
- Groenewegen M.A.T., Whitelock P.A., Smith C.H., Kerschbaum F. 1998, MNRAS 293, 18
- Habing H.J. 1996, A&ARv 7, 97
- Habing H.J., Tignon J., Tielens A.G.G.M. 1994, A&A 286, 523
- Herman J., Habing H.J. 1985, A&AS 59, 523
- Kim S., Staveley-Smith L., Dopita M.A., et al. 1998, ApJ 503, 674
- Lequeux J., Le Bourlot J., Pineau Des Forêts G., et al. 1994, A&A 292, 371
- Lindqvist M., Winnberg A., Habing H.J., Matthews H.E. 1992, A&AS 92, 43
- Loup C., Zijlstra A.A., Waters L.B.F.M., Groenewegen M.A.T. 1997, A&AS 125, 419
- Netzer N., Knapp G.R. 1987, ApJ 323, 734
- Richards A.M.S., Yates J.A., Cohen R.J. 1998, MNRAS 299, 319
- Richards A.M.S., Yates J.A., Cohen R.J. 1999, MNRAS 306, 954
- Sjouwerman L.O., van Langevelde H.J., Winnberg A., Habing H.J. 1998, A&AS 128, 35
- Stanimirović S., Staveley-Smith L., Dickey J.M., Sault R.J., Snowden S.L. 1999, MNRAS 302, 417
- Struck C., Smith D.C., Willson L.A., Turner G., Bowen G.H. 2004, MNRAS in press
- Takaba H., Ukita N., Miyaji T., Miyoshi M. 1994, PASJ 46, 629
- te Lintel Hekkert P., Caswell J.L., Habing H.J., Haynes R.F., Norris R.P. 1991, A&AS 90, 327
- Trams N.R., van Loon J.Th., Waters L.B.F.M., et al. 1999, A&A 346, 843
- van Langevelde H.J., Janssens A.M., Goss W.M., Habing H.J., Winnberg A. 1993, A&AS 101, 109
- van Loon J.Th. 2000, A&A 354, 125
- van Loon J.Th. 2002, in: IAU Colloquium 185, eds. C. Aerts, T.R. Bedding & J. Christensen-Dalsgaard. ASP Conf.Proc. Vol. 259, p548
- van Loon J.Th., Zijlstra A.A., Bujarrabal V., Nyman L.-Å. 1996, A&A 306, L29
- van Loon J.Th., Zijlstra A.A., Whitelock P.A., et al. 1998a, A&A 329, 169
- van Loon J.Th., te Lintel Hekkert P., Bujarrabal V., Zijlstra A.A., Nyman L.-Å. 1998b, A&A 337, 141
- van Loon J.Th., Groenewegen M.A.T., de Koter A., et al. 1999, A&A 351, 559
- van Loon J.Th., Zijlstra A.A., Kaper L., et al. 2001a, A&A 368, 239
- van Loon J.Th., Zijlstra A.A., Bujarrabal V., Nyman L.-Å. 2001b, A&A 368, 950
- van Loon J.Th., Marshall J.R., Matsuura M., Zijlstra A.A. 2003, MNRAS 341, 1205
- Vlemmings W.H.T., van Langevelde H.J., Diamond P.J. 2002, A&A 393, L33
- Vlemmings W.H.T., van Langevelde H.J., Diamond P.J., Habing H.J., Schilizzi R.T. 2003, A&A 407, 213
- Whitelock P.A., Feast M.W., Menzies J.W., Catchpole R.M. 1989, MNRAS 238, 769
- Whitelock P.A., Feast M.W., van Loon J.Th., Zijlstra A.A. 2003, MNRAS 342, 86
- Wood P.R., Bessel M.S., Whiteoak J.B. 1986, ApJ 306, L81
- Wood P.R., Whiteoak J.B., Hughes S.M.G., et al. 1992, ApJ 397, 552
- Wood P.R., Habing H.J., McGregor P.J. 1998, A&A 336, 925
- Zijlstra A.A., Loup C., Waters L.B.F.M., et al. 1996, MNRAS 279, 32
- Zijlstra A.A., Chapman J.M., te Lintel Hekkert P., et al. 2001, MNRAS 322, 280